Characterization of Multicellular Niches Supporting Hematopoietic Stem Cells Within Distinct Zones

Ruochen Dong[1], Hua Li[1], Xi C He[1], Chen Wang[2], Anoja Perera[1], Seth Malloy[1], Jonathon Russell[1], Wenting Li[1], Kaitlyn Petentler[1], Xinjian Mao[1], Zhe Yang[1], Michael Epp[1], Kate Hall[1], Allison Scott[1], Sarah E Smith[1], Mark Hembree[1], Yongfu Wang[1], Sean McKinney[1], Jeff Haug[1], Jay Unruh[1], Brian Slaughter[1], Xunlei Kang[2], Linheng Li[1,3,4*]

[1]Stowers Institute for Medical Research, Kansas City, MO 64110, USA

[2] Division of Hematology and Oncology, Department of Medicine, University of Missouri School of Medicine, Columbia, MO 65212, USA

[3]Department of Pathology & Laboratory Medicine, Molecular Oncology, University of Kansas Medical Center, Kansas City, Kansas, 66160, USA

[4]Lead Contact

*Correspondence: lil@stowers.org (L.L.)

Abstract

Previous studies of hematopoietic stem cells (HSCs) primarily focused on single cell-based niche models, yielding fruitful but conflicting findings[1-5]. Here we report our investigation on the fetal liver (FL) as the primary fetal hematopoietic site using spatial transcriptomics. Our study reveals two distinct niches: the portal-vessel (PV) niche and the sinusoidal niche. The PV niche, composing N-cadherin (N-cad)^{Hi}Pdgfrα^{+} mesenchymal stromal cells (MSCs), endothelial cells (ECs), and N-cad^{Lo}Albumin^{+} hepatoblasts, maintains quiescent and multipotential FL-HSCs. Conversely, the sinusoidal niche, comprising ECs, hepatocytes, and potential macrophages, supports proliferative FL-HSCs biased towards myeloid lineages. Unlike prior reports on the role of Cxcl12, with its depletion from vessel-associated stromal cells leading to 80% of HSCs' reduction in the adult bone marrow (BM)[6,7], depletion of *Cxcl12* via *Cdh2*^{CreERT} (encoding N-cad) induces FL-HSCs relocation from the PV to the sinusoidal niches, resulting in an increase of myeloid-biased HSCs. Similarly, we discovered that adult BM encompasses two niches within different zones, each composed of multi-cellular components: trabecular bone area (TBA, or metaphysis) supporting deep-quiescent HSCs, and central marrow (CM, or diaphysis) fostering relatively proliferative HSCs. This study transforms our understanding of niches by shifting from single cell-based to multicellular components within distinct zones, illuminating the intricate regulation of HSCs tailored to their different cycling states.

Introduction

Hematopoietic stem cells (HSCs) possess the remarkable self-renew ability and multilineage potential, ensuring a lifelong supply of both HSCs and lineage cells[8]. Definitive HSCs emerge from the hemogenic endothelium in the aorta-gonad-mesonephros (AGM) region around E10.5-11.5 and subsequently migrate to the FL after E12.5 for expansion. The FL serves as the primary site for

HSC maturation and expansion[9-12]. It is estimated that HSCs undergo a 38-fold expansion between E12 and E18 in the FL before migrating to the BM after E16.5 to support lifelong hematopoiesis in adults[13-15].

In the adult BM, it was proposed that HSCs reside within physically confined microenvironment or niche[16], however the identification of the cell types that serve as niches in supporting HSCs within the BM has been a long journey over the past two decades[1-4,17]. The first HSC niche was found in the TBA or metaphysis as evidenced by the observations that increased TBA led to an increased HSC number[18,19], thus forming the concept of the endosteal (inner bone surface) niche. Notably, in these studies, long-term (LT) quiescent HSCs were identified using two criteria: 1) LT BrdU labeling (for 10-days) followed by a 70-day chase to detect label-retaining cells (LRCs), and 2) HSC markers $Lin^{-}CD45^{+}Sca1^{+}Kit^{+}$ expression in a subset of LRCs. Within the increased TBA, more N-cad^{+} bone-lining cells correlates with more $LRC^{+}Lin^{-}CD45^{+}Sca1^{+}Kit^{+}$ HSCs[18]. It is important to acknowledge that employing different LRC procedures, including variations in labeling and chasing time, may result in the identification of different cell status or even cell types[20]. This is because each division of HSCs diminishes their labels such as BrdU or GFP and their self-renewal capacity, and it should be noted that not all LRCs necessarily correspond to HSCs[21,22]. Moreover, these LT quiescent HSCs were primarily found in the endosteal region (70-75%) and within the TBA, many of which were observed adjacent to N-cad^{+} bone-lining cells, although the exact nature of the latter was not fully understood at the time[18,21,23]. Functionally, through the utilization of real-time imaging technology, transplanted HSCs were often detected homing to the endosteal region, particularly to the N-cad^{+} niche within the TBA[24,25]. With the identification of improved HSC markers, $Lin^{-}CD150^{+}CD48^{-}CD41^{-}$, the more accurate mapping the location of HSCs became possible as 1 out of 3 $CD150^{+}CD48^{-}CD41^{-}$ cells were shown to support LT multilineage reconstitution in the repopulation assay[26]. Utilizing Immunofluorescent staining with $Lin^{-}CD150^{+}CD48^{-}CD41^{-}$ markers, HSCs were confirmed to localize in the endosteal niche (~14-16%), but a large portion of these

phenotypical HSCs (80-85%) were found within 5-cell distance from blood vessel, especially the sinusoid, thus the vascular niche concept was formed[26,27]. Subsequently, numerous groups have contributed to identification of various cell types that provide a niche function and these include Cxcl12-Aboundandt Reticular (CAR) cells, Nonmyelin Schwann cells, Nestin^{+}, Prx1^{+}, or Leptin receptor (LepR)$^{+}$ stromal cells, as well as megakaryocytes (Mks)[7,27-33]. Given that the majority of stromal cells as described above are associated with vessels, and the main components of which are the sinusoidal structure primarily found within the CM covered by compact bone in the diaphysis region, the concept of the perivascular niche predominantly confined within the CM has emerged[5]. Consistent with the observation that ~85% HSCs reside in the perivascular niche, deletion of *Cxcl12* or *KitL* (or SCF) from vessel and vessel-associated stromal, such as LepR^{+} or Prx1^{+}, cells, led to a substantial (~85%) loss of HSCs[6,7,34]. However, the location and characteristics of the remaining HSCs after the depletion of HSCs from the CM remained largely unclear. The following observation seems to provide an answer: myeloablation induced by the chemotherapy agent 5-fluorouracil (5-FU) resulted in a significant loss of HSCs primarily residing in perivascular niches, whereas the surviving, thus reserve, HSCs predominantly (~75%) found in the endosteal niche within TBA[35].

Among the cell types reported with niche functions, accumulating evidence strongly supports mesenchymal stem cells (MSCs) as pivotal in maintaining HSCs[28]. Several MSC markers have been identified within BM, including Nestin, Prx1, and LepR [7,28,30]. While N-cad was the first identified niche mark in BM, the characteristic of N-cad^{+} stromal cells was not fully understood until they were revealed to possess the potential to differentiate into not only osteoblasts but also adipocytes and chondrocytes, thus validating N-cad as an MSC marker[35]. All of the aforementioned studies shed light on niche markers and factors, providing valuable insights into understanding FL-HSCs and their interactions with niches.

While the FL primarily acts as a temporary site for HSC further maturation and expansion, numerous studies have focused on identifying the cellular and molecular components involved in supporting FL-HSC expansion. Previous investigations, primarily utilizing histological staining, *in vitro* culture, and single-cell RNA sequencing (scRNA-seq), have revealed complex interactions between FL-HSCs and various FL cell types, including ECs, hepatoblasts, hepatic stellate (stromal) cells, perivascular cells, and macrophages, mediated by diverse cytokines and chemokines[36-42]. Despite the undeniable roles of different FL structure cells and hematopoietic cells in supporting FL-HSCs, it still requires a systematic and comprehensive understanding of the niches responsible for FL-HSC maintenance and expansion.

Histological imaging, while capable of showing cell positions, often revealing only a limited set of markers. Single cell (sc)RNA-seq can provide an in-depth profile of gene expression but lacks the ability to preserve the spatial information of each cell within its original tissue context, making it challenging to comprehensively profile the HSC-niche interactions and signaling. In contrast, high-resolution spatial transcriptomics represents a promising and cutting-edge technology that integrates spatial information with transcriptomic data[43]. This approach enables the profiling of gene expression within their native spatial context, providing a powerful way to visualize gene expression patterns within a tissue or organ with unprecedented detail[43,44]. Hence, in this study, we employed high-resolution spatial transcriptomics, specifically the Slide-seq V2 method[45], to generate a spatial transcriptomic cell atlas of the mouse FL. Additionally, we utilized genetic approaches to validate our observations derived from spatial transcriptomics. Our primary objective was to investigate the niches responsible for maintaining and expanding FL-HSCs.

Results

Single-cell RNA-seq reveals the transcriptomics of mouse fetal live HSCs and potential niche cells.

To establish a comprehensive cell atlas of HSCs and other cell types in FL, we

conducted scRNA-seq of the mouse FL at E16.5. Given the rarity in the FL, we first isolated HSCs using fluorescence-activated cell sorting (FACS) and then combined them with $CD45^-$ non-hematopoietic cells and $CD45^+$ hematopoietic cells from the E16.5 FLs for scRNA-seq analysis, resulting in a total of 62,236 collected cells[46]. Subsequently, we employed the Uniform Manifold Approximation and Projection (UMAP) analysis to identify and classify 8 clusters of FL parenchymal cells and 22 clusters of hematopoietic cells (Fig. 1a). Through a differential expressed gene (DEG) analysis, we uncovered marker genes specific to HSCs as well as potential niche cells (Fig. 1b). Notably, we observed high expression levels of *Ifitm1*, *Hoxa7*, *Hoxa9*, *Cd27*, *Kit*, and *Ltb* in E16.5 FL-HSCs. Additionally, we found that well-known HSC surface markers, such as *Procr* (Epcr), *Ly6a* (Sca1), and *Slamf1* (CD150), were also enriched in E16.5 FL-HSCs (Fig. 1c). We examined gene expressions in various potential niche cell types, including MSCs, ECs, hepatoblasts/hepatocytes, megakaryocytes, and macrophages. FL-MSCs displayed enrichment of *Pdgfr*α, *Pdgfr*β, *Acta2*, *Fgfr1*, and *Col1a1*. We then compared several known MSC markers in adult BM. *Nestin* and *Cspg4* (encoding Ng2) were previously reported to be expressed in arterial pericytes that located in proximity to FL-HSCs and exhibited the ability to drive HSC expansion *in vitro*[38]. Our data showed that only a subset of FL-MSCs expressed with either *Nes* (39.87%) or *Cspg4* (Ng2) (10.66%). In fact, *Nestin* was predominantly expressed in endothelial cells. Similarly*, Lepr* was predominantly enriched in endothelial cells[30] and barely detected in MSCs (0.71%) (Fig. 1d). We discovered that *Cdh2* (N-cad) was highly expressed in MSCs (59.77%) and to a lesser extend in hepatoblasts, displaying an expression pattern largely overlapping with that of *Cxcl12* in both MSCs (75.00%) and hepatoblasts (Fig. 1e). Additionally, other Niche factors, such as *Kitl* and *Igf2,* were found in both MSCs and hepatoblasts; but *Ptn and Thpo* were respectively detected in MSCs and hepatoblasts.

We also conducted immunofluorescence staining to gain further insights into the cellular structure of the PV region of E14.5 FL. We identified four major cell types in the peri-PV region: inner layer comprised of $Endomucin^+/CD31^+$ ECs; the outer layer

consisted of N-cad^{High}Pdgfrα^{+} MSCs; and surrounded by N-cad^{Low} Albumin^{+} hepatoblasts. Notably, the majority of MSCs were observed adjacent to PV ECs in the peri-PV region (Fig. 1f, Extended Data Fig. 1a-d). For comparison, Nestin expression was detected in Endomucin^{+} ECs and a subset of N-cad^{High} MSCs (Extended Data Fig. 1e, f). Previously, FL stellate cells or perivascular mesenchymal cells with expression of Desmin and Acta2 were shown to play a role in supporting FL-HSCs [40]. In line with this report, our scRNA-seq and IF staining results revealed that N-cad^{Hi}MSCs exhibited an enrichment of Desmin (Extended Data Fig. 1g, h).

In summary, we have effectively generated a fully annotated single-cell resolution atlas of the mouse FL at E16.5, together with IF staining, we provided comprehensive insights into the cellular architecture of FL structure cells in the peri-portal vessel region (Fig. 1g). Notably, our study unveils that N-cad-expressing cells constitute the primary source of niche factors in mouse FL.

High-resolution spatial transcriptomics identifies HSCs and niche cells in mouse FL.

To gain a comprehensive understanding of the interactions between HSCs and niche cells, we employed Slide-seq V2, a high-resolution (10μm) spatial transcriptomic technology in our study [45]. We collected two sections of E14.5 mouse FL, focusing specifically on a region enriched with portal vessels, as previous studies have suggested proximity of FL-HSCs to the PV structure (Fig. 2a, b, Extended Data Fig. 2a). Since Slide-seq had not been previously applied to mouse FL investigations, we conducted quality control analyses by assessing raw reads, high-quality reads, and exotic reads, and compared them with a previous study conducted on the mouse hippocampus[44] (Extended Data Fig. 2b-e). Our Slide-seq data exhibited a median of approximately 320 unique molecular identifiers (UMI) per bead (d=10μm) and a median of around 240 genes per bead, with minimal reads corresponding to ribosomal genes (Extended Data Fig. 2i-l). Initially, using UMAP analysis, we identified only 10 distinct cell clusters due to the lower UMI and gene reads compared

to scRNA-seq (Extended Data Fig. 2 f-g). To construct a comprehensive high-resolution spatial transcriptomic atlas of the E14.5 mouse FL, we applied the Robust Cell Type Decomposition (RCTD) algorithm to assign cell types to the beads based on expression profiles derived from E14.5 scRNA-seq[47]. This supervised approach facilitated the categorization of 28 cell types, including 24 hematopoietic cell types and 4 parenchymal cell types (Extended Data Fig. 2 h).

We initially detected the presence of signature genes associated with erythrocytes and erythroblasts across the entire "puck"(a rubber-coated glass coverslip containing a monolayer of randomly deposited, DNA barcoded beads)[43] (Extended Data Fig. 3a). As anticipated, the signature genes specific to the main structural and functional cells in the FL, such as hepatoblasts and their progeny hepatocytes, were predominantly detected within the tissue-covered regions (Extended Data Fig. 3b). To investigate the spatial distribution of FL cells and the interaction between HSCs and niche cells, we assigned the beads as credible representatives of a specific cell type when the enriched signature genes exceeded a certain threshold. For potential niche cells, we first annotated hepatoblasts and hepatocytes using a threshold of 25%, which best represented the spatial localization of these cell types on the puck (Extended Data Fig. 3c, d). Utilizing this threshold, we identified five potential niche cell populations on the pucks, each displaying its distinct spatial distribution pattern. Specifically, hepatoblasts and hepatocytes were major parenchymal cells in the liver responsible for supporting structural and metabolic functions (Fig. 2c). Furthermore, we observed an enrichment of MSCs in the PV region, consistent with our prior IF staining findings (Fig. 2d). Most megakaryocytes and macrophages were distributed within the liver lobes. ECs either resided on the border of the PV as PV-ECs or were dispersed within the lobe as sinusoid ECs, most of them are localized at the distal region (Fig. 2 e-g). A total of 7 HSCs were identified on puck #1, and 5 HSCs were identified on puck #2 using a threshold of 35% (Fig. 2h, Extended Data Fig. 3e). Previous studies from Ema et al. and Khan JA et al. estimated that the total number of FL-HSCs is ~500 at E14 and ~1100 at E15, and FL-HSCs are enriched surrounding portal vessel[13,38]. Based on the thickness of our section (10um) and an average of 6 FL-HSCs identified

per section, we estimated that the total number of FL-HSCs per E14.5 liver in our experiment is less than 1200, which is close to previous findings. It is noteworthy that the majority of HSCs were found in close proximity to MSCs within the PV regions (Fig. 2i, Extended Data Fig. 3f). Out of the 12 HSCs from both pucks, 7 were adjacent to MSCs, 5 were near ECs, 4 were close to hepatoblasts, 1 was in proximity to megakaryocytes, and none were near macrophages. To assess the significant enrichment of HSCs to niche cells considering the variable abundance of niche cell types in the FL, we performed a permutation test (see method). The results showed a significant enrichment of FL-HSCs near MSCs and ECs compared to other cell types (Fig. 2j, Extended Data Fig. 3g). Furthermore, to comprehensively explore the niche cells surrounding each HSC, we applied a decomposition method to identify the niche cell identities on each bead within a radius of 50μm or 30μm from each HSC. Our analysis consistently revealed that 8 out of 12 HSCs were located within a compartment enriched with MSCs, while 4 out of 12 HSCs resided in a compartment enriched with hepatoblasts and hepatocytes. In fact, 6 out of 12 HSCs tended to be in direct contact with MSCs. (Fig. 2k, Extended Data Fig. 4a-e). Immunofluorescence staining subsequently provided visual evidence of close spatial proximity between a $Lin^{-}CD48^{-}CD150^{+}$ HSC and the N-cad^{Hi} MSCs as the outer layer of PV, as well as the $CD31^{+}$ EC as the inner layer of PV (Fig. 2l).

To compare with a previous study that utilized the 10x Visium spatial transcriptomics solution for investigating FL-HSCs[41], we employed the same method to three consecutive slices from an E14.5 mouse FL, following the standard protocol[41]. The 10x Visium method yielded an average of 5,139 median UMI per spot (d=55μm) and 1,756 median genes per spot, which were substantially lower than those obtained with SLIDE-seq (5,139 vs 320, d=55μm vs d=10μm; 1,756 vs 240, d=55μm vs d=10μm). Initially, the 10x Visium analysis identified nine cell clusters (Extended Data Fig. 5a, b). Consistently, MSCs were enriched in the PV region, exhibiting a gene enrichment score of approximately 80%, while megakaryocytes were predominantly located in the liver lobe region, with a gene enrichment score of around 30% (Extended Data Fig. 5c, d). However, the 10x Visium approach identified an average

of two binding spots per section containing HSCs, with a gene enrichment score below 25% (Extended Data Fig. 5e). Similarly, to Slide-seq findings, the majority (4 out of 6) of HSC-containing binding spots were found adjacent to or overlapping with MSC-containing binding spots.

In summary, our high-resolution Slide-seq approach facilitated the generation of a comprehensive spatial transcriptomic map of the mouse FL at E14.5. In addition, the anatomical delineation of the PV structure through IF staining depicted MSCs and ECs respectively forming the outer and inner layers of PV. Collectively, our analyses unveiled a significant enrichment of FL-HSCs within the PV region, positioned directly adjacent to MSCs and indirectly influenced by signaling emanating from ECs. While the enrichment of FL-HSCs to hepatoblasts didn't reach statistical significance, the abundance of the latter suggests a potential interaction between them.

Slide-seq decodes HSC-niche interactions.

To investigate the dynamics of FL-HSCs and niche cells across various developmental stages, we performed unsupervised scRNA-seq clustering using a dataset comprising 50,804 cells obtained from FACS-sorted $CD45^+$ and $CD45^-$ populations at E14.5, E16.5, and E18.5 (Fig. 3a, Extended Data Fig. 6a). The differential expression of genes (DEG) analysis was conducted to identify representative genes of HSCs at the three embryonic time points. Notably, at E18.5, FL-HSCs exhibited a higher proportion of cycling cells, indicated by increased expression of *Mki67*, and decreased expression of *Cdkn1c (p57)*, *H19,* and *Mpl*. Previous studies have shown roles of *Cdkn1c (p57)*, *H19,* and *Mpl* in the maintenance of quiescent HSCs in the adult BM[48-50]. Additionally, we observed upregulation of FL-HSC signature genes such as *Procr*, *Hoxa9*, *Kit*, and *Mecom* during late gestation. However, genes associated with differentiation, including *Flt3*, and *Tgfβr1*, also showed increased expression levels. Consistently, we found a notable increase in the frequency of Pre-B and B cells, accompanied by a decrease in the frequency of HSCs and megakaryocytes from E14.5 to E18.5, which are

consistent with the gradual increase of *Flt3* but decrease of *Mpl* and *Tek*[23,50,51] (Fig. 3 b, c).

To explore the potential ligand-receptor interactions between niche cells and HSCs in an unbiased manner, we utilized CellPhone DataBase (CPDB) analysis[52]. Specifically, we focused on characterizing interactions between HSCs and potential niche cells, including MSCs, ECs, hepatoblasts, megakaryocytes, and macrophages. Through comprehensive analysis, we identified MSCs as the primary providers of ligands involved in niche-HSC interactions. These included well-established niche signals known to support HSC in the adult BM, such as *Cxcl12-Cxcr4*, *Cxcl12-Dpp4*, *Igf1-Igf1r*, *Igf2-Igf2r*, *Dlk1-Notch1/2*, *Tgfβs-Tgfβrs*, *Ptn-Ptprs*, *Kitl-kit*, and *Wnt* signaling pathways. Hepatoblasts shared most of the identified interactions with MSCs, apart from their unique enrichment in the *Thpo-Mpl* signaling module with HSCs, suggesting their role in supporting megakaryocyte fate. ECs shared several ligands with MSCs, including *Bmp4-Acvr2b*, *Kitl-Kit*, *Igf1-Igf2r*, *Igf2-Igf2r*, *Tgfβ2-Tgfβr2/3*, and *Ptn-Ptprs, but* lacked *Cxcl12-Cxcr4*, *Cxcl12-Dpp4*, and *Dlk1-Notch1/2* signaling modules. In fact, only N-cad-expressing cells, including MSCs and hepatoblasts, exhibited a *Cxcl12-Cxcr4* interaction, suggesting their role as major chemokine-releasing cells involved in HSC homing and localization. Macrophages and megakaryocytes displayed several distinct interactions respectively, including *Ifng-Ifitm1* and *Pf4-Cxcr3 respectively*, suggesting their unique contributions to support FL-HSCs (Fig. 3d).

While CPDB offers a scRNA-seq-based method for predicting ligand-receptor interactions between cell clusters, it lacks the ability to provide a spatial representation of genuine cell-cell interactions within an anatomically organized tissue. To verify the cell-cell interactions identified by CPDB analysis, we first employed a "projection" model to enhance genes detected on slide-seq (Extended Data Fig. 6b). Next, we assessed the "observed" expression profile of *Alb*, which ranked as the 3rd most enriched gene on the puck and compared it with the "projected" expression profile. The projection model effectively enhanced the expression level of *Alb* with high fidelity (Extended Data Fig. 6c-f). Similarly, the

expression profile of *Cxcl12*, previously known to be enriched in MSCs, was significantly enhanced using the projection model (Extended Data Fig. 6 g, h). We then utilized Slide-seq to examine the spatial expression patterns of the ligand-receptor pairs predicted by CPDB analysis. Based on the number of HSCs involved in ligand-receptor interactions with niche cells, we defined these interactions as strong (involving at least 3 out of 7 HSCs, Extended Data Fig. 7a, b, f, j), weak (involving 1 or 2 out of 7 HSCs, Extended Data Fig. 7c, d, h, i), or no interaction (Extended Data Fig. 7e, j). Overall, MSCs exhibited several strong interactions with HSCs, including *Cxcl12-Cxcr4*, *Ptn-Ptprs*, *Kitl-Kit*, *Tgfβ2-Tgfβr2*, and *Dlk1-Notch1/2*. Additionally, MSCs displayed weak interactions such as *Cxcl12-Dpp4*, *Flt3l-Flt3*, *Igf1/2-Igfr1/2*, *Tgfβ1-Tgfβr1*, *Tgfβ3-Tgfβr3*, *Bmp4-Acvr2b*, *Bmp5-Bmpr2*, *Angptl2-Tie2*, *Wnt2-Fzd6*, and *Wnt5a-Celsr1/Fzd6/Ryk* (Fig. 3e-i, Extended Data Fig. 7k). These findings indicate that MSCs are a major source of niche factors that maintain FL-HSCs in proximity.

The depletion of Cxcl12 from N-cad-expressing cells leads to increased frequency of HSCs exhibiting lineage-biased differentiation.

It has been established that Cxcl12 serves a crucial niche factor for maintaining HSCs in the adult BM, demonstrated by studies showing that the loss of Cxcl12 from BM vessel and vessel-associated stromal cells resulted a large reduction of HSC frequency[7]. Given our observation that *Cxcl12-Cxcr4* interactions exclusively occur between HSCs and N-cad-expressing cells, including MSCs and hepatoblasts, we generated a conditional *Cxcl12* knockout mouse model using the $Cdh2^{CreERT}$;$Cxcl12^{f/f}$ strain to investigate the role of Cxcl12 in the maintenance of HSCs in the FL (Fig. 4a). Subsequently, we performed fluorescence-activated cell sorting assays to assess the impact of Cxcl12 loss on the frequency of HSCs, B cells, and $CD41^+$ megakaryocytes (Extended Data Fig. 8a). Unexpectedly, conditional knockout of Cxcl12 from N-cad-expressing cells resulted in a significant (approximately 2-fold) increase in HSCs when normalized to $CD45^+$ cells (~1.5-fold increase normalized to total liver

cells) (Fig. 4b). FL B cells were completely depleted upon loss of Cxcl12 (Fig. 4c). Conversely, the number of megakaryocytes increased significantly (~2-fold) when normalized to $CD45^+$ cells (Fig. 4d).

Consistently, scRNA-seq analysis revealed that the loss of Cxcl12 had a significant impact on HSC proliferation as evidenced by increased HSC number and skewed lineage differentiation. Specifically, there was an increased myeloid cell such as megakaryocytes and their progenitors, Inversely, there were loss of common lymphoid progenitors (CLPs) and B lymphocytes upon conditional knockout of Cxcl12 from N-cad-expressing cells (Fig. 4e, f). DEG analysis showed that Cathepsin G (*Ctsg)*, *Mpo*, Selectin L (*Sell)*, and *Tetherin* were increased in HSCs after Cxcl12 loss, providing the molecular basis for an increase in HSC proliferation, mobilization, as well as an increase in differentiation towards myeloid cells [53-56] (Fig. 4g). Moreover, Gene ontology (GO) analysis revealed an enrichment of pathways related to NADH regeneration and glycolysis in HSCs upon Cxcl12 loss (Fig. 4h). N-cad-expressing cells, particularly MSCs together with ECs, hepatoblasts in the PV niche, are responsible for maintaining FL-HSCs with their full lineage potential. DEG analysis of MSCs revealed that MSCs in wild-type (WT) mice are enriched in *Igf1* and *Cxcl12*, indicative of their supportive role in HSC maintenance[57] (Extended Data Fig. 8b). Subsequently GO analysis indicated that MSCs in WT mice are enriched in pathways related to extracellular matrix organization and collagen fibril organization, suggesting that extracellular remodeling by MSCs may create a favorable microenvironment with appropriate geometric and mechanical properties to harbor HSCs[58] (Extended Data Fig. 8c). In contrast, MSCs in conditional knockout (cKO) mice lost the enrichment of extracellular matrix organization pathways, indicating an unfavorable extracellular matrix microenvironment for HSCs harbor (Extended Data Fig. 8d).

Based on the CPDB analysis, the predicted significant ligand-receptor signaling from MSCs to HSCs, including *Dlk1-Notch1/2*, *Ptn-Ptprs*, *Cxcl12-Cxcr4*, *Cxcl12-Dpp4*, and *Igf1-Igf1r*, were reduced following the cKO of *Cxcl12*. Of particular note, the *Flt3l-Flt3* signaling module between MSCs and HSCs was lost, most likely responsible for loss of CLP and downstream B cells[59]. Several other ligand-receptor signaling interactions

between potential niche cells and HSCs were also found to be reduced, such as *Pf4-Cxcr3* and *C5ar1-Rps19* between Megakaryocyte and HSCs, *Igf1-Igf1r* and *C5ar1-Rps19* between Kupffer cells and HSCs, and *Cxcl12-Cxcr4* between hepatoblasts and HSCs. Furthermore, *Tgfβ* signaling was predicted to be increased in hepatoblasts/ hepatocytes and Kupffer cells, while *Thpo-Mpl* signaling was increased in hepatoblasts/hepatocytes, suggesting their involvement in skewed myeloid differentiation[60,61]. Moreover, endothelial cells showed an increase in *Sirpa-Cd47* signaling, implying the potential involvement of immune privilege pathways to safeguard FL-HSCs against macrophage clearance and potentially contribute to HSC expansion[62] (Extended Data Fig. 8e).

To further investigate the functional significance of Cxcl12 originating from N-cad-expressing cells in HSC maintenance, we isolated FL-HSCs from both WT and *Cxcl12*-cKO mice and transplanted them into WT adult recipient mice, which possess a normal expression of Cxcl12 from N-cad-expressing cells. Following 16-week period, we observed that the recipient mice exhibited balanced lineage reconstitution, indicating that the observed lineage bias resulted from *Cdh2*^{CreER} induced *Cxcl12* depletion in the FL was a niche-dependent phenotype (Fig. 4i).

The absence of Cxcl12 from N-cad-expressing cells results in the altered localization of HSCs to distinct niches.

As Cxcl12-Cxcr4 constitutes a well-known chemoattractant signaling pathway, we hypothesized that the loss of Cxcl12 from N-cad-expressing cells would lead to the relocation of HSCs. To test this, we employed Slide-seq using two FL sections from E16.5 WT and *Cxcl12*-cKO mice, respectively. Consistent with our previous findings in E14.5 mouse FL, HSCs were notably enriched in the PV region and located close to MSCs in E16.5 FL (Fig. 5a). As anticipated, the depletion of Cxcl12 from N-cad^{+} cells resulted in the relocation of HSCs (Fig. 5b). Specifically, in WT mice, 50% ± 23% of 36 HSCs were found within 50μm of MSCs, whereas, in *Cxcl12*-cKO mice, only 13% ± 3% HSCs were in proximity to MSCs. Similarly, in WT mice, 73% ± 9% of HSCs

were close to ECs, compared to 38% ± 9% HSCs in *Cxcl12*-cKO mice (Fig. 5c, d). To assess the significance of HSC enrichment in proximity to various niche cells, we conducted a permutation test. The data revealed that HSCs in WT mice were significantly enriched in proximity to MSCs and ECs, whereas HSCs in *Cxcl12*-cKO mice did not show such enrichment. Although the frequency of HSCs in proximity to ECs decreased after Cxcl12 knockout, permutation tests indicated that the enrichment of HSCs in proximity to ECs did not change significantly between WT and cKO mice (Fig. 5e, Extended Data Fig. 9a). These findings suggest that the relocation of HSCs away from MSCs and remain interaction with ECs at distal-to-PV regions. Furthermore, the data showed that hepatoblasts are more enriched at portal vessel region, whereas hepatocytes are relatively enriched at distal region. Interestingly, at portal vessel region, HSCs in both WT and cKO are interacted with hepatoblast cell-enriched neighbor. On the contrary, at sinusoid regions, HSCs tended to interact with hepatocyte-enriched neighbor. This data suggests that the Cxcl12 low expressing hepatocytes attract the homing of HSCs to the sinusoidal niche after deletion of Cxcl12 from N-Cad-expressing cells (MSCs and hepatoblast cells). In addition, the distinct niche comprised of ECs and abundant hepatocytes is responsible for FL-HSC expansion.

Since FL-HSCs predominantly undergo proliferation, we further subclustered the E16.5 HSCs into cycling and non-cycling populations based on their gene expression profiles from scRNA-seq (Extended Data Fig. 9b-d). The non-cycling HSCs exhibited high levels of *Cdkn1c (p57)*, *Ctnnal1(α-catenin1)*, and *H19*, indicative of their quiescent state. We then mapped the location of cycling and non-cycling HSCs in the E16.5 FL (Extended Data Fig. 9e-h). The frequency of cycling HSCs was increased upon Cxcl12 loss, which is consistent with the expansion of HSCs (Extended Data Fig. 10a).

Our findings indicate that the PV niche consisting of MSCs, ECs, and potentially hepatoblasts in mouse FL plays a crucial role in maintaining relatively non-cycling HSCs with full lineage potential. The loss of Cxcl12 from N-cad-expressing cells leads to the migration of FL-HSCs towards a distal sinusoidal niche, which comprising ECs

and potentially abundant hepatocytes but lacking MSCs (Extended Fig. 10d). Occasionally, megakaryocytes and macrophages can also be part of sinusoidal nice. The sinusoidal niche is pivotal in supporting proliferation of HSCs, albeit with a myeloid-lineage bias.

The absence of Cxcl12 from N-cad-expressing cells results in the relocation of BM HSCs from trabecular bone region to central marrow region.

Intriguingly, we discovered that the model of two HSC niches within distinct zones can also be observed in mouse bone marrow. We transplanted $1x10^6$ total nucleated bone marrow cells isolated from mT/mG mice into WT recipient (n=6), or the recipient with conditional knockout (cKO) of Cxcl12 from N-cadherin-expressing cells (n=5). After 8 weeks, the femur was collected from both groups and IF staining of td-tomato was used to identify the distribution of transplanted donor cells. The distribution of transplanted donor cells was significantly enriched in the trabecular bone area (TBA, or metaphysis) in Wt recipients. Upon conditional knockout of Cxcl12 from N-cadherin-expressing cells, transplanted donor cells tended to home to the central marrow (CM, or diaphysis) and showed a more evenly distribution across BM (Fig. 6f, g). FASC analysis of the bone marrow from both groups showed that the LSK cell number was significantly increased in cKO mice compared to WT mice (9.49% vs 3.25%), indicating that CM niche supports the proliferation of HSPCs (Fig. 6h). We further conducted cell cycle analysis on the LSK cell in both groups. Data showed that in WT mice, in which the majority of HSCs reside in TBA area, 59.19% LSK cells are in G0 phase, 28.43% LSK cells are in G1 phase, and 7.74% LSK cells are in G2/S/M phase. As a comparison, LSK cells in cKO mice exhibited a more proliferative profile, with 38.65% LSK cells are in G0 phase, 29.08% LSK cells are in G1 phase, and 25.42% LSK cells are in G2/S/M phase (Fig. 6i). In summary, similar to our finding in mouse fetal liver, mouse bone marrow also existed distinct niches, which are consisted of multicellular components at distinct zones (CM vs TBA), rather than a single cells-based niche, regulate the homing and localization of HSCs and tailor them to their different cycling states.

Discussion

The journey of identifying and characterizing niches supporting HSCs has been lengthy and intricate, marked by significant progress but often filled with conflicting findings over the past decades. This complexity stems from both the complicated nature of the BM system, and the predominant influence of the single cell-based niche model in exploring HSC niches, resulted in a complex and sometimes controversial understanding of cell types crucial for HSC maintenance and function[1-5]. The first niche discovered as supportive of HSCs in the adult mouse BM was the endosteal niche, situated within the TBA[18,19]. This niche, primarily composed of either osteogenic lineage or N-cad-expressing bone lining cells that now are recognized as MSCs[63], was found to support LT quiescent HSCs[18,63]. Functional assays such as transplantation or myeloablation experiments using 5-FU demonstrated the crucial role of the endosteal niche, especially within the TBA, in attracting homing of HSCs or supporting the survival of HSCs in response to severe stress [35]. This aligns with the notion that the endosteal niche predominantly supports a 'dormant' (deep quiescent) state of HSCs, functioning as a reserve pool[18,21,64].

Subsequent studies uncovered additional HSC niches within the adult BM, including the vascular niche, which *per se* occupies approximately 25% of the entire BM volume[65] and hosts around 80-85% of HSCs[26,27]. The majority vessels, especially mature sinusoidal vessels, are predominantly covered by compact bone correlating to the diaphysis region and largely confined within the CM. Various cell types, particularly in the perivascular region, such as CAR cells, Schwann cells, and MSCs expressing Nestin, Lepr, or Prx1, contribute to niche functions[7,23,27-31,63,66,67]. Deletion experiments targeting molecules like Cxcl12 or Kitl from these vessels and vessel-associated MSCs, or myeloablation using 5-FU, resulted in a significant (80-85%) reduction of HSCs, underscoring the importance of these niches in supporting HSCs [6,7,34,35].

In contrast to the adult BM, FL-HSCs were thought to have unique proliferative features, suggesting a distinct niche microenvironment[68]. Prior studies have revealed

potential niche cell types in FL, including arteriolar ECs, PV-associated stroma cells, and macrophages[38,41,42]. Recent studies have shed light on FL-HSC behavior, suggesting a bias towards differentiation rather than self-renewal[69]. Utilizing high-resolution spatial transcriptomics technology, our study uncovered existing two niches at different zones of FL. The PV niche, located at the central region connecting four lobes of FL, composed of MSCs, ECs, and hepatoblasts, plays a critical role in maintaining quiescent HSCs with full lineage potential. Conversely, the sinusoidal niche, located at the distal-to-PV region within FL lobes and comprising ECs and hepatocytes, supports proliferative HSCs with a bias towards myeloid lineage. Moreover, Cxcl12, known as a niche-maintaining factor in adult BM, functions as a conventional chemoattractant. Loss of Cxcl12 from N-cad-expressing niche cells leads to altered locations of HSCs from the initial PV to the sinusoidal niches, at the latter HSCs exhibiting an “aging” phenotype: increased proliferation but with myeloid bias.

These findings not only refine our understanding of FL-HSC niches in separating maintenance from supporting proliferation of HSCs but also have implications for adult BM. Unexpectedly, depletion of Cxcl12 from N-cad^{+} endosteal niche in adult BM did not lead to loss of HSCs rather changed the location of homed HSCs from TBA to the CM. This observation enabled us to uncover two-niches with multiple cellular components within distinct zones in adult BM. Within the TBA, besides N-cad^{+} MSCs and osteogenic cells at the endosteal region, other niche cell components, including various types of ECs such as arteriolar ECs and capillaries, and neural cells, contribute to HSC regulations[70,71]. Similarly, within the CM, in addition to abundant sinusoidal ECs, there are vessel-associated MSCs, Schwann cells, and MKs, all contributing to niche function[7,23,27-31,63,66,67]. The TBA zone supports deep quiescent and multipotential HSCs, whereas CM zone seems to support relatively active HSCs. TGFβ1 produced mainly from MKs and activated by Schwann cells, maintains a temporal quiescent state of HSCs during homeostasis but supports HSC restoration post BM injury via FGF signaling [29,31,61]. Consistently in a recent elegant study, imaging of myelopoiesis defined the anatomy of normal and stress hematopoiesis

near megakaryocytes [72].

In summary, while spatial transcriptomics has advanced our understanding of HSC niche interactions, challenges remain, particularly regarding the cellular and molecular mechanisms underlying the discrepancy between the wide distribution of Cxcl12 in both FL or BM but the specific homing of HSCs to the PV or endosteal niche within TBA? This is not simply due to the sensitivity of the vessel to the irradiation procedure required for transplantation assay since HSCs alternatively home to the CM when Cxcl12 was deleted from the N-cad^{+} niche within the TBA. Nevertheless, this comprehensive analysis represents paradigm shift regarding the niche concept from single cell-based to multicellular components within distinct zones, reflecting the intricate regulation of HSCs in response to their different cycling states and metabolic activities, offering valuable insights for hematopoietic homeostasis, aging process, and leukemogenesis.

ACKNOWLEDGMENTS

We thank K. Ferro, K. Bae, F. Liu, Z. Yu, E. Hamilton, M. Treese, I. Dunwiddie, J. Morrison, and M. Peterson, M. Miller for technical support.

We would like to acknowledge the Board Institute and Dr. Fei Chen's group for providing the Slide-seq V2 pucks.

We would like to acknowledge the University of Kansas Medical Center's Genomics Core for their support in generating data on the Illumina NovaSeq 6000 System. The core is supported by the following grants: Kansas Intellectual and Developmental Disabilities Research Center (NIH U54 HD 090216), the Molecular Regulation of Cell Development and Differentiation – COBRE (P30 GM122731-03) and the NIH S10 High-End Instrumentation Grant (NIH S10OD021743)"

AUTHOR CONTRIBUTIONS: R.D. conceived the project, designed, and performed experiments, analyzed data, and wrote the manuscript. H.L and J.R. performed bioinformatics analysis. R.D., W.L., S.M., K.P., K.H., A.S, Y.W., and S.M. performed scRNA-seq, Slide-seq, immunofluorescence staining, and 10X Visium experiments.

X.C.H. and M.H. provided the training. W.L., X.M., Z.Y., and M.E. contributed to animal work. M.E. performed proof-reading of the manuscript. S.S., S.M., Y.W., A.P., J.H., J.U., and B.S. provided technical assistance. L.L. and X.C.H. supervised the study and revised the manuscript.

DECLARATION OF INTERESTS

The authors declare no competing interests.

Method (main text):

Mice

The mice utilized in this study were all housed in the AAALAC-accredited animal facility located at the Stowers Institute for Medical Research (SIMR), and were handled according to both SIMR and National Institutes of Health guidelines. All procedures involving experimental animals were approved and authorized by the Institutional Animal Care and Use Committee (IACUC) of SIMR. N-cad-CreER^{T} mice were generated by Applied StemCell, Inc. To induce N-cad-CreER^{T}; Cxcl12 f/f mouse, Tamoxifen (Sigma) was injected intraperitoneally to the pregnant mothers at 2mg per injection at E10.5, E12.5, and E14.5. C57BL/6, Ptprc, and Cxcl12 floxed mice were acquired from the Jackson Laboratory.

Tissue preparation and handling

FL tissue was received freshly harvested in 1x PBS and were individually submerged in OCT to remove excess PBS. Tissues were moved to a cryo-mold with fresh OCT and orientated in “tulip” orientation for transverse tissue sectioning. Tissue blocks were then flash frozen at -70°C before sectioning (HistoChill, Novec™ 7000). Region of interest (multiple portal/central vein openings on same plain) were identified prior to tissue capture.

ScRNA-Seq

Dissociated cells in PBS + 2.5% FBS were assessed for concentration and viability via a Luna-FL cell counter (Logos Biosystems). Cells deemed to be 75-98% viable were loaded on a Chromium Single Cell Controller (10x Genomics), based on live cell concentration. Libraries were prepared using either the Chromium Single Cell 3' Reagent Kits v3 or the Chromium Next GEM Single Cell 3' Reagent Kits v3.1 (10x Genomics) according to manufacturer's directions. Libraries were sequenced to a depth necessary to achieve at least 18,000 mean reads per cell on an Illumina NovaSeq6000 or Illumina NextSeq500.

Slide-seq V2

The Slide-seq pucks used in this study were generated and sequenced at the Broad Institute (Cambridge, MA) by Dr. Fei Chen's group according to the methods and Extended Data information provided in the Nature Biotechnology publication "Highly sensitive spatial transcriptomics at near-cellular resolution with Slide-seq V2" [44]. The spatial barcode sequencing file of the pucks were generated via monobase ligation chemistry and provided by Dr. Chen's group to be used for later analysis. The tissue was sectioned to 10 µm thickness and mounted directly onto the pucks using a cryostat (CryoStar NX70). Subsequent library preparation was performed according to manufacturer's directions for the Nextera XT kit (Illumina, FC-131-1096)

10x Visium

Four 10um-thick tissue sections were adhered to the barcoded spots within the four individual capture areas of a 10x Genomics Visium Spatial Gene Expression Slide. The tissue was permeabilized for 18 minutes then processed to create cDNA and next generation sequencing libraries according to manufacturer's instructions for the Visium Spatial Gene Expression Reagent and Slide Kits (10x Genomics, PN-1000189 and PN-1000188). Libraries were pooled at equal molar concentrations and sequenced to a depth necessary to achieve at least 50,000 read pairs per tissue covered spot on the Illumina NextSeq 500 instrument using a High Output flow cell.

Flow Cytometry

Cells from mouse FLs or recipient BM freshly collected in 1xPBS with 2.5% PBS. Cells were then stained with surface markers for 30 min at 4°C and washed with PBS (with 2.5% FBS) trice. Cells were then stained with 7-ADD/DAPI for 5 mins on ice and then analyzed by ZE5 (Bio-Rad) or sorted by S6 cell sorter (BD Biosciences). FAC express software 7.0 was used for data analysis.

For cell cycle analysis, BM cells were fixed in 4% PFA at room temperature for 30min, followed by surface marker staining for 30 min at 4°C. Cells were then incubated with anti-Ki67 in 1xPBS+0.1% tween-20 overnight at 4°C, followed by DAPI staining for 5 min on ice and then analyzed by ZE5 (Bio-Rad).

Fluorescence-activated cell sorting was performed on S6 cell sorter (BD Biosciences) for the enrichment of HSC and niche cells for scRNA-seq. $Cd150^{+}$, $EPCR^{+}$, $N\text{-}cad^{+}$, $CD31^{+}$ cells were collected and pooled with $CD45^{+}$ and $CD45^{-}$ cell for scRNA-seq.

Bioinformatics and Statistical analysis

To determine whether certain niche cell types are in the same niche micro-environment and in proximity to HSCs, we applied a permutation test. First, a fixed number equal of beads are randomly selected from all beads for a given puck and annotated as “pseudo” HSCs. The number of the “pseudo” HSCs are equal to the number of “real” HSCs identified on each puck. Second, beads and their annotated cell types within a 50um radius centered to the “pseudo” HSCs are identified. Finally, the number of niche cells are counted with each of these micro-environments (50um circle). This process was repeated 100 times, and the proportion of the number of nearby niche cells that are more extreme than our observed one is calculated. This proportion is the p-value showing how often the HPSCs and niche cells are in proximity.

See Extended Data method for the full bioinformatics analytical methods.

Figure Legends

Fig. 1. scRNA-seq profiling of E16.5 mouse FL reveals markers for FL-HSCs and potential niche cells.

(a) UMAP visualization of E16.5 FL depicting distinct populations of HSCs and FL structure cells.

(b) Dot plot representation displaying marker genes for HSCs and potential niche cells.

(c) UMAP plot highlighting signature genes specific to HSCs.

(d) UMAP plot showcasing signature genes specific to FL structure cells.

(e) UMAP plot indicating the expression of niche factors in potential niche cells.

(f) Immunofluorescence staining demonstrating the cellular architecture surrounding a portal vessel. Solid arrow: Pecam1^{+} endothelial cells; Solid arrowhead: N-cad^{High} Pdgfrα^{+} MSCs; Hollow arrow: N-cad^{Low} Hepatoblasts. Two peri-PV regions (A)(B) were highlighted and zoomed on the right panels.

(g) Illustrations depicting the cellular architecture adjacent to a portal vessel.

Fig. 2. Mapping cellular architecture and interactions in E14.5 mouse FL using Slide-seq.

(a) Illustrations depicting the mouse FL and plane of sections.

(b) DAPI staining on pre-puck section (left), the reconstructed SLIDE-seq puck

post-sequencing (Middle), and the alignment of the tissue on the puck (Right).

(c)-(g) Identification of hepatoblasts & hepatocytes, MSCs, endothelial cells, megakaryocytes, and macrophages (Kupffer cells) using Slide-seq with a threshold of 25% (15% for endothelial cells).

(h) Identification of HSCs with a threshold of 35%.

(i) Cellular architecture of E14.5 mouse FL. Circles highlight the FL-HSCs.

(j) Permutation test demonstrating the enrichment of HSCs to potential niche cells. The closest niche cell within 50μm to HSCs was considered as the niche cell to HSCs.

(k) Bar graph presenting the average cell identities surrounding each HSC from puck#1 within 50μm. Decomposition was applied to all the beads surrounding each HSC within 50μm. The weights of erythrocytes and erythroblasts were excluded on all the beads.

(l) Immunofluorescence staining illustrating the HSCs-MSC interactions. Solid red arrow: $CD150^{+}Lin^{-}CD48^{-}CD41^{-}$ HSC; hollow red arrow: $CD150^{+}LIN^{+}CD48^{+}CD41^{+}$ Hematopoietic progenitor and lineage cells; red arrowhead: N-cad^{High} MSCs; yellow arrowhead: $Pecam1^{+}$ endothelial cells.

***, $p<0.001$.

Fig. 3. Predicting ligand-receptor interactions between niche cells and HSCs using Cellphone DB and SLIDE-seq.

(a) Combined UMAP of mouse E14.5, E16.5, and E18.5 FL

(b) Dot plot illustrating the changes in HSC signature genes across mouse E14.5, E16.5, and E18.5 FL.

(c) Bar plot displaying the frequency of HSCs and lineage cells in mouse E14.5, E16.5, and E18.5 FL.

(d) Cellphone DB analysis predicting niche-HSC signaling in E14.5, E16.5, and E18.5 mouse FL.

(e) - (i) Slide-seq revealing the signaling interactions between MSCs and HSCs in

E14.5 mouse FL.

Fig. 4. Conditional knockout of Cxcl12 from N-cad expressing cells leads to HSC expansion with myeloid bias.

(a) Schematic overview of the experimental workflow.

(b) - (d) Representative FACS profiles and bar plots demonstrating the expansion of HSCs (b), depletion of B cells (c), and increased megakaryocytes (d) following the loss of Cxcl12 from N-cad-expressing cells.

(e) UMAP visualization of E16.5 mouse FL from wild-type (WT) and conditional knockout (cKO) mice.

(f) Bar plot indicating the skewed myeloid differentiation after the loss of Cxcl12 from N-cad expressing cells.

(g) Volcano plot displaying differentially expressed genes (DEGs) in HSCs mediated by Cxcl12 cKO from N-cad-expressing cells.

(h) Bubble plot illustrating the top Gene Ontology (GO) terms in HSCs (BP: biological process; CC: cellular components; MF: Molecular Functions) affected by Cxcl12 cKO from N-cad-expressing cells.

(i) Bar plot showing the frequency of B cells, T cells, and myeloid cells in the recipient BM 16 weeks post-transplantation.

*, $p<0.05$; **, $p<0.01$; ***, $p<0.001$.

Fig. 5. Slide-seq reveals the relocation of mouse FL-HSCs after conditional knockout of Cxcl12 from N-cad-expressing cells.

(a) (b) Slide-seq images displaying the cellular architecture in E16.5 mouse FL from wild-type (WT) (a) and conditional knockout (cKO) (b) mice (hepatoblasts and hepatocytes not shown).

(c) Bar plot illustrating the distances between HSCs and MSCs in WT and cKO mice.

(d) Bar plot indicating the significance of HSCs located within a distance of <50μm to niche cells in WT and cKO mice.

(e) Permutation test demonstrating the enrichment of total HSCs in proximity to potential niche cells in WT and cKO mice.

(f) Immunofluorescent staining of td-tomato showing the distribution of donor bone marrow cells (from mT/mG mice) in the recipient bone marrow after 8 weeks. Yellow dots showing the td-tomato+ donor cells by using anti-td-tomato IF staining.

(g) Bar plot indicating the distribution of td-tomato+ donor bone marrow cells in the three different regions of recipient bone marrow.

(h) FASC analysis and bar plot showing the proportion of LSK cells in recipient bone marrow in control vs cKO mice.

(i) FASC analysis and bar plot showing the cell cycle analysis of LSK cells in recipient bone marrow in control vs cKO mice.

*, $p<0.05$; ***, $p<0.001$. (e) showing combined p-value calculated using Fisher's combined probability test of 2 permutation tests on 2 pucks of WT, and cKO.

(g) showing combined p-value calculated using student-t's test.

References

1 Li, L. & Xie, T. STEM CELL NICHE: Structure and Function. *Annual review of cell and developmental biology* **21**, 605-631 (2005).

2 Hoggatt, J., Kfoury, Y. & Scadden, D. T. Hematopoietic Stem Cell Niche in Health and Disease. *Annu Rev Pathol* **11**, 555-581 (2016).

3 Torres, L. S. *et al.* Recent advances in "sickle and niche" research - Tribute to Dr. Paul S Frenette. *Stem cell reports* **17**, 1509-1535 (2022).

4 Yang, Z., Dong, R., Mao, X., He, X. C. & Li, L. Stress-protecting harbors for hematopoietic stem cells. *Current opinion in cell biology* **86**, 102284 (2024).

5 Morrison, S. J. & Scadden, D. T. The bone marrow niche for haematopoietic stem cells. *Nature* **505**, 327-334 (2014).

6 Ding, L. & Morrison, S. J. Haematopoietic stem cells and early lymphoid progenitors occupy distinct bone marrow niches. *Nature* **495**, 231-235 (2013).

7 Greenbaum, A. *et al.* CXCL12 in early mesenchymal progenitors is required for haematopoietic

763 stem-cell maintenance. *Nature* **495**, 227-230 (2013).
764 8 Weissman, I. L. & Shizuru, J. A. The origins of the identification and isolation of hematopoietic stem
765 cells, and their capability to induce donor-specific transplantation tolerance and treat autoimmune
766 diseases. *Blood* **112**, 3543-3553 (2008).
767 9 Müller, A. M., Medvinsky, A., Strouboulis, J., Grosveld, F. & Dzierzakt, E. Development of
768 hematopoietic stem cell activity in the mouse embryo. *Immunity* **1**, 291-301 (1994).
769 10 de Bruijn, M. F., Speck, N. A., Peeters, M. C. & Dzierzak, E. Definitive hematopoietic stem cells first
770 develop within the major arterial regions of the mouse embryo. *EMBO J* **19**, 2465-2474 (2000).
771 11 Kumaravelu, P. *et al.* Quantitative developmental anatomy of definitive haematopoietic stem
772 cells/long-term repopulating units (HSC/RUs): role of the aorta-gonad-mesonephros (AGM) region and
773 the yolk sac in colonisation of the mouse embryonic liver. *Development* **129**, 4891-4899 (2002).
774 12 Medvinsky, A. & Dzierzak, E. Definitive hematopoiesis is autonomously initiated by the AGM region.
775 *Cell* **86**, 897-906 (1996).
776 13 Ema, H. & Nakauchi, H. Expansion of hematopoietic stem cells in the developing liver of a mouse
777 embryo. *Blood* **95**, 2284-2288 (2000).
778 14 Christensen, J. L., Wright, D. E., Wagers, A. J. & Weissman, I. L. Circulation and chemotaxis of fetal
779 hematopoietic stem cells. *PLoS Biol* **2**, E75 (2004).
780 15 Gekas, C., Dieterlen-Lièvre, F., Orkin, S. H. & Mikkola, H. K. The placenta is a niche for hematopoietic
781 stem cells. *Dev Cell* **8**, 365-375 (2005).
782 16 Schofield, R. The relationship between the spleen colony-forming cell and the haemopoietic stem cell.
783 *Blood Cells* **4**, 7-25 (1978).
784 17 Crane, G. M., Jeffery, E. & Morrison, S. J. Adult haematopoietic stem cell niches. *Nat Rev Immunol* **17**,
785 573-590 (2017).
786 18 Zhang, J. *et al.* Identification of the haematopoietic stem cell niche and control of the niche size.
787 *Nature* **425**, 836-841 (2003).
788 19 Calvi, L. M. *et al.* Osteoblastic cells regulate the haematopoietic stem cell niche. *Nature* **425**, 841-846
789 (2003).
790 20 Kokkaliaris, K. D. *et al.* Adult blood stem cell localization reflects the abundance of reported bone
791 marrow niche cell types and their combinations. *Blood* **136**, 2296-2307 (2020).
792 21 Wilson, A. *et al.* Hematopoietic Stem Cells Reversibly Switch from Dormancy to Self-Renewal during
793 Homeostasis and Repair. *Cell* **135**, 1118-1129 (2008).
794 22 Bernitz, J. M., Kim, H. S., MacArthur, B., Sieburg, H. & Moore, K. Hematopoietic Stem Cells Count and
795 Remember Self-Renewal Divisions. *Cell* **167**, 1296-1309 e1210 (2016).
796 23 Arai, F. *et al.* Tie2/angiopoietin-1 signaling regulates hematopoietic stem cell quiescence in the bone
797 marrow niche. *Cell* **118**, 149-161 (2004).
798 24 Xie, Y. *et al.* Detection of functional haematopoietic stem cell niche using real-time imaging. *Nature*
799 **457**, 97-101 (2009).
800 25 Lo Celso, C. *et al.* Live-animal tracking of individual haematopoietic stem/progenitor cells in their niche.
801 *Nature* **457**, 92-96 (2009).
802 26 Kiel, M. J., Yilmaz, O. H., Iwashita, T., Terhorst, C. & Morrison, S. J. SLAM family receptors distinguish
803 hematopoietic stem and progenitor cells and reveal endothelial niches for stem cells. *Cell* **121**,
804 1109-1121 (2005).
805 27 Sugiyama, T., Kohara, H., Noda, M. & Nagasawa, T. Maintenance of the hematopoietic stem cell pool
806 by CXCL12-CXCR4 chemokine signaling in bone marrow stromal cell niches. *Immunity* **25**, 977-988

807 (2006).
808 28 Méndez-Ferrer, S. *et al.* Mesenchymal and haematopoietic stem cells form a unique bone marrow
809 niche. *Nature* **466**, 829-834 (2010).
810 29 Yamazaki, S. *et al.* Nonmyelinating Schwann cells maintain hematopoietic stem cell hibernation in the
811 bone marrow niche. *Cell* **147**, 1146-1158 (2011).
812 30 Zhou, B. O., Yue, R., Murphy, M. M., Peyer, J. G. & Morrison, S. J. Leptin-receptor-expressing
813 mesenchymal stromal cells represent the main source of bone formed by adult bone marrow. *Cell*
814 *Stem Cell* **15**, 154-168 (2014).
815 31 Zhao, M. *et al.* Megakaryocytes maintain homeostatic quiescence and promote post-injury
816 regeneration of hematopoietic stem cells. *Nat Med* **20**, 1321-1326 (2014).
817 32 Bruns, I. *et al.* Megakaryocytes regulate hematopoietic stem cell quiescence through CXCL4 secretion.
818 *Nat Med* **20**, 1315-1320 (2014).
819 33 Nakamura-Ishizu, A., Takubo, K., Fujioka, M. & Suda, T. Megakaryocytes are essential for HSC
820 quiescence through the production of thrombopoietin. *Biochem Biophys Res Commun* **454**, 353-357
821 (2014).
822 34 Ding, L., Saunders, T. L., Enikolopov, G. & Morrison, S. J. Endothelial and perivascular cells maintain
823 haematopoietic stem cells. *Nature* **481**, 457-462 (2012).
824 35 Zhao, M. *et al.* N-Cadherin-Expressing Bone and Marrow Stromal Progenitor Cells Maintain Reserve
825 Hematopoietic Stem Cells. *Cell Rep* **26**, 652-669.e656 (2019).
826 36 Chou, S. & Lodish, H. F. Fetal liver hepatic progenitors are supportive stromal cells for hematopoietic
827 stem cells. *Proc Natl Acad Sci U S A* **107**, 7799-7804 (2010).
828 37 Sugiyama, D., Kulkeaw, K., Mizuochi, C., Horio, Y. & Okayama, S. Hepatoblasts comprise a niche for
829 fetal liver erythropoiesis through cytokine production. *Biochem Biophys Res Commun* **410**, 301-306
830 (2011).
831 38 Khan, J. A. *et al.* Fetal liver hematopoietic stem cell niches associate with portal vessels. *Science* **351**,
832 176-180 (2016).
833 39 Tan, K. S., Kulkeaw, K., Nakanishi, Y. & Sugiyama, D. Expression of cytokine and extracellular matrix
834 mRNAs in fetal hepatic stellate cells. *Genes to Cells* **22**, 836-844 (2017).
835 40 Kordes, C., Sawitza, I., Götze, S. & Häussinger, D. Hepatic stellate cells support hematopoiesis and are
836 liver-resident mesenchymal stem cells. *Cell Physiol Biochem* **31**, 290-304 (2013).
837 41 Gao, S. *et al.* Identification of HSC/MPP expansion units in fetal liver by single-cell spatiotemporal
838 transcriptomics. *Cell Res* **32**, 38-53 (2022).
839 42 Lu, Y. *et al.* Spatial transcriptome profiling by MERFISH reveals fetal liver hematopoietic stem cell niche
840 architecture. *Cell Discovery* **7**, 47 (2021).
841 43 Rodriques, S. G. *et al.* Slide-seq: A scalable technology for measuring genome-wide expression at high
842 spatial resolution. *Science (New York, N.Y* **363**, 1463-1467 (2019).
843 44 Stickels, R. R. *et al.* Highly sensitive spatial transcriptomics at near-cellular resolution with Slide-seqV2.
844 *Nat Biotechnol* **39**, 313-319 (2021).
845 45 Marshall, J. L. *et al.* High-resolution Slide-seqV2 spatial transcriptomics enables discovery of
846 disease-specific cell neighborhoods and pathways. *iScience* **25**, 104097 (2022).
847 46 Weksberg, D. C., Chambers, S. M., Boles, N. C. & Goodell, M. A. CD150- side population cells represent
848 a functionally distinct population of long-term hematopoietic stem cells. *Blood* **111**, 2444-2451 (2008).
849 47 Cable, D. M. *et al.* Robust decomposition of cell type mixtures in spatial transcriptomics. *Nature*
850 *Biotechnology* **40**, 517-526 (2022).

851 48 Matsumoto, A. *et al.* p57 is required for quiescence and maintenance of adult hematopoietic stem
852 cells. *Cell Stem Cell* **9**, 262-271 (2011).
853 49 Venkatraman, A. *et al.* Maternal imprinting at the H19–Igf2 locus maintains adult haematopoietic
854 stem cell quiescence. *Nature* **500**, 345-349 (2013).
855 50 Yoshihara, H. *et al.* Thrombopoietin/MPL signaling regulates hematopoietic stem cell quiescence and
856 interaction with the osteoblastic niche. *Cell Stem Cell* **1**, 685-697 (2007).
857 51 Sitnicka, E. *et al.* Complementary signaling through flt3 and interleukin-7 receptor alpha is
858 indispensable for fetal and adult B cell genesis. *J Exp Med* **198**, 1495-1506 (2003).
859 52 Efremova, M., Vento-Tormo, M., Teichmann, S. A. & Vento-Tormo, R. CellPhoneDB: inferring cell–cell
860 communication from combined expression of multi-subunit ligand–receptor complexes. *Nature*
861 *Protocols* **15**, 1484-1506 (2020).
862 53 Florez, M. A. *et al.* Interferon Gamma Mediates Hematopoietic Stem Cell Activation and Niche
863 Relocalization through BST2. *Cell Rep* **33**, 108530 (2020).
864 54 Pellin, D. *et al.* A comprehensive single cell transcriptional landscape of human hematopoietic
865 progenitors. *Nature Communications* **10**, 2395 (2019).
866 55 Upadhaya, S. *et al.* Kinetics of adult hematopoietic stem cell differentiation in vivo. *J Exp Med* **215**,
867 2815-2832 (2018).
868 56 Schroeder, T. & Just, U. Notch signalling via RBP-J promotes myeloid differentiation. *EMBO J* **19**,
869 2558-2568 (2000).
870 57 Young, K. *et al.* Decline in IGF1 in the bone marrow microenvironment initiates hematopoietic stem
871 cell aging. *Cell Stem Cell* **28**, 1473-1482 e1477 (2021).
872 58 Oswald, J. *et al.* Gene-Expression Profiling of CD34+ Hematopoietic Cells Expanded in a Collagen I
873 Matrix. *Stem Cells* **24**, 494-500 (2006).
874 59 Sitnicka, E. *et al.* Key role of flt3 ligand in regulation of the common lymphoid progenitor but not in
875 maintenance of the hematopoietic stem cell pool. *Immunity* **17**, 463-472 (2002).
876 60 de Sauvage, F. J. *et al.* Stimulation of megakaryocytopoiesis and thrombopoiesis by the c-Mpl ligand.
877 *Nature* **369**, 533-538 (1994).
878 61 Challen, G. A., Boles, N. C., Chambers, S. M. & Goodell, M. A. Distinct hematopoietic stem cell
879 subtypes are differentially regulated by TGF-beta1. *Cell stem cell* **6**, 265-278 (2010).
880 62 Jaiswal, S. *et al.* CD47 is upregulated on circulating hematopoietic stem cells and leukemia cells to
881 avoid phagocytosis. *Cell* **138**, 271-285 (2009).
882 63 Zhao, M. *et al.* N-Cadherin-Expressing Bone and Marrow Stromal Progenitor Cells Maintain Reserve
883 Hematopoietic Stem Cells. *Cell Rep* **26**, 652-669 e656 (2019).
884 64 Haug, J. S. *et al.* N-cadherin expression level distinguishes reserved versus primed states of
885 hematopoietic stem cells. *Cell stem cell* **2**, 367-379 (2008).
886 65 Nombela-Arrieta, C. & Manz, M. G. Quantification and three-dimensional microanatomical
887 organization of the bone marrow. *Blood Adv* **1**, 407-416 (2017).
888 66 Kunisaki, Y. *et al.* Arteriolar niches maintain haematopoietic stem cell quiescence. *Nature* **502**,
889 637-643 (2013).
890 67 Kiel, M. J. *et al.* SLAM family receptors distinguish hematopoietic stem and progenitor cells and reveal
891 endothelial niches for stem cells. *Cell* **121**, 1109-1121 (2005).
892 68 Gao, S. & Liu, F. Fetal liver: an ideal niche for hematopoietic stem cell expansion. *Sci China Life Sci* **61**,
893 885-892 (2018).
894 69 Ganuza, M. *et al.* Murine foetal liver supports limited detectable expansion of life-long

895 haematopoietic progenitors. *Nat Cell Biol* **24**, 1475-1486 (2022).
896 70 Shahrabi, S., Rezaeeyan, H., Ahmadzadeh, A., Shahjahani, M. & Saki, N. Bone Marrow Blood Vessels:
897 Normal and Neoplastic Niche. *Oncol Rev* **10**, 306 (2016).
898 71 Ho, Y. H. *et al.* Remodeling of Bone Marrow Hematopoietic Stem Cell Niches Promotes Myeloid Cell
899 Expansion during Premature or Physiological Aging. *Cell stem cell* **25**, 407-418 e406 (2019).
900 72 Wu, Q. *et al.* Resilient anatomy and local plasticity of naive and stress haematopoiesis. *Nature* **627**,
901 839-846 (2024).
902

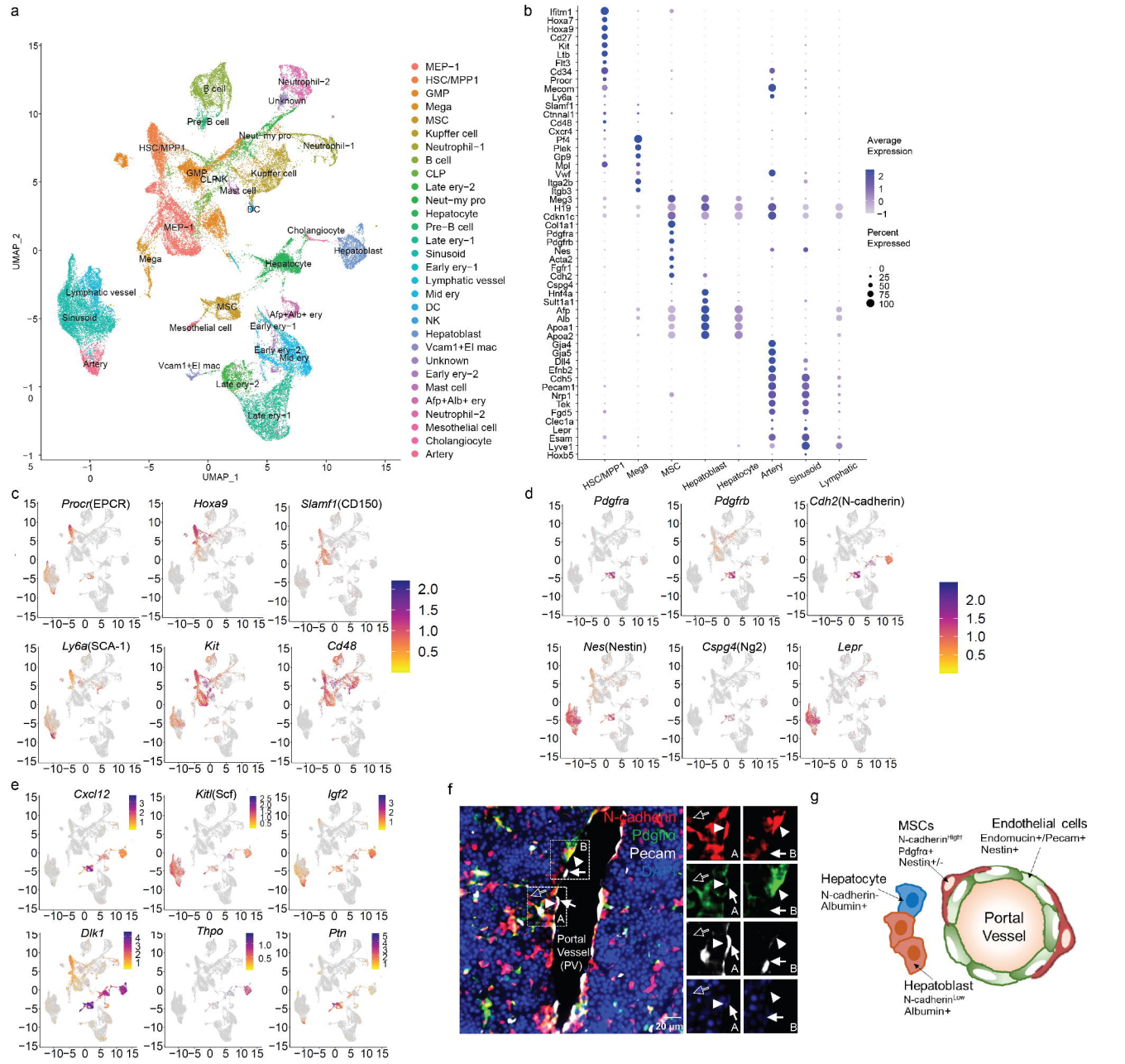
a
UMAP_1
UMAP_2
MEP−1
HSC/MPP1
GMP
Mega
MSC
Kupffer cell
Neutrophil−1
B cell
CLP
Late ery−2
Neut−my pro
Hepatocyte
Pre−B cell
Late ery−1
Sinusoid
Early ery−1
Lymphatic vessel
Mid ery
DC
NK
Hepatoblast
Vcam1+El mac
Unknown
Early ery−2
Mast cell
Afp+Alb+ ery
Neutrophil−2
Mesothelial cell
Cholangiocyte
Artery
b
Average Expression
Percent Expressed
HSC/MPP1
Mega
MSC
Hepatoblast
Hepatocyte
Artery
Sinusoid
Lymphatic
c
Procr(EPCR)
Hoxa9
Slamf1(CD150)
Ly6a(SCA-1)
Kit
Cd48
d
Pdgfra
Pdgfrb
Cdh2(N-cadherin)
Nes(Nestin)
Cspg4(Ng2)
Lepr
e
Cxcl12
Kitl(Scf)
Igf2
Dlk1
Thpo
Ptn
f
N-cadherin
Pdgfrb
Pecam
DAPI
Portal Vessel (PV)
20 μm
g
MSCs
N-cadherin^High
Pdgfra+
Nestin+/-
Endothelial cells
Endomucin+/Pecam+
Nestin+
Hepatocyte
N-cadherin-
Albumin+
Portal Vessel
Hepatoblast
N-cadherin^Low
Albumin+

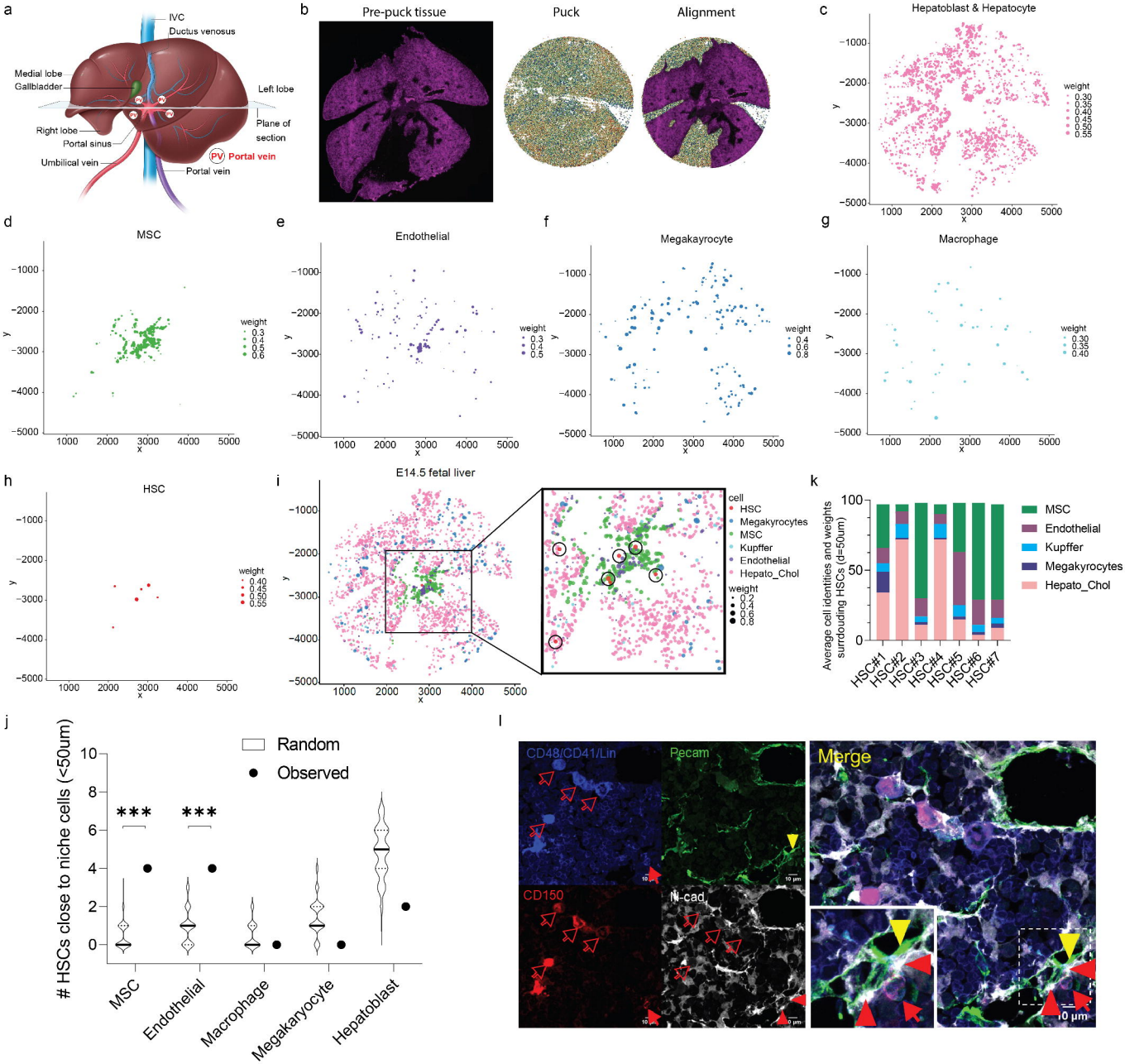
a
IVC
Ductus venosus
Medial lobe
Gallbladder
Left lobe
Plane of section
Right lobe
Portal sinus
Umbilical vein
PV Portal vein
Portal vein
b
Pre-puck tissue
Puck
Alignment
c
Hepatoblast & Hepatocyte
weight
0.30
0.35
0.40
0.45
0.50
0.55
d
MSC
e
Endothelial
f
Megakayrocyte
g
Macrophage
h
HSC
i
E14.5 fetal liver
cell
HSC
Megakyrocytes
MSC
Kupffer
Endothelial
Hepato_Chol
weight
k
Average cell identities and weights surrouding HSCs (d=50um)
MSC
Endothelial
Kupffer
Megakyrocytes
Hepato_Chol
HSC#1
HSC#2
HSC#3
HSC#4
HSC#5
HSC#6
HSC#7
j
Random
Observed
HSCs close to niche cells (<50um)
***
***
MSC
Endothelial
Macrophage
Megakanyocyte
Hepatoblast
l
CD48/CD41/Lin
Pecam
Merge
CD150
N-cad
10 µm

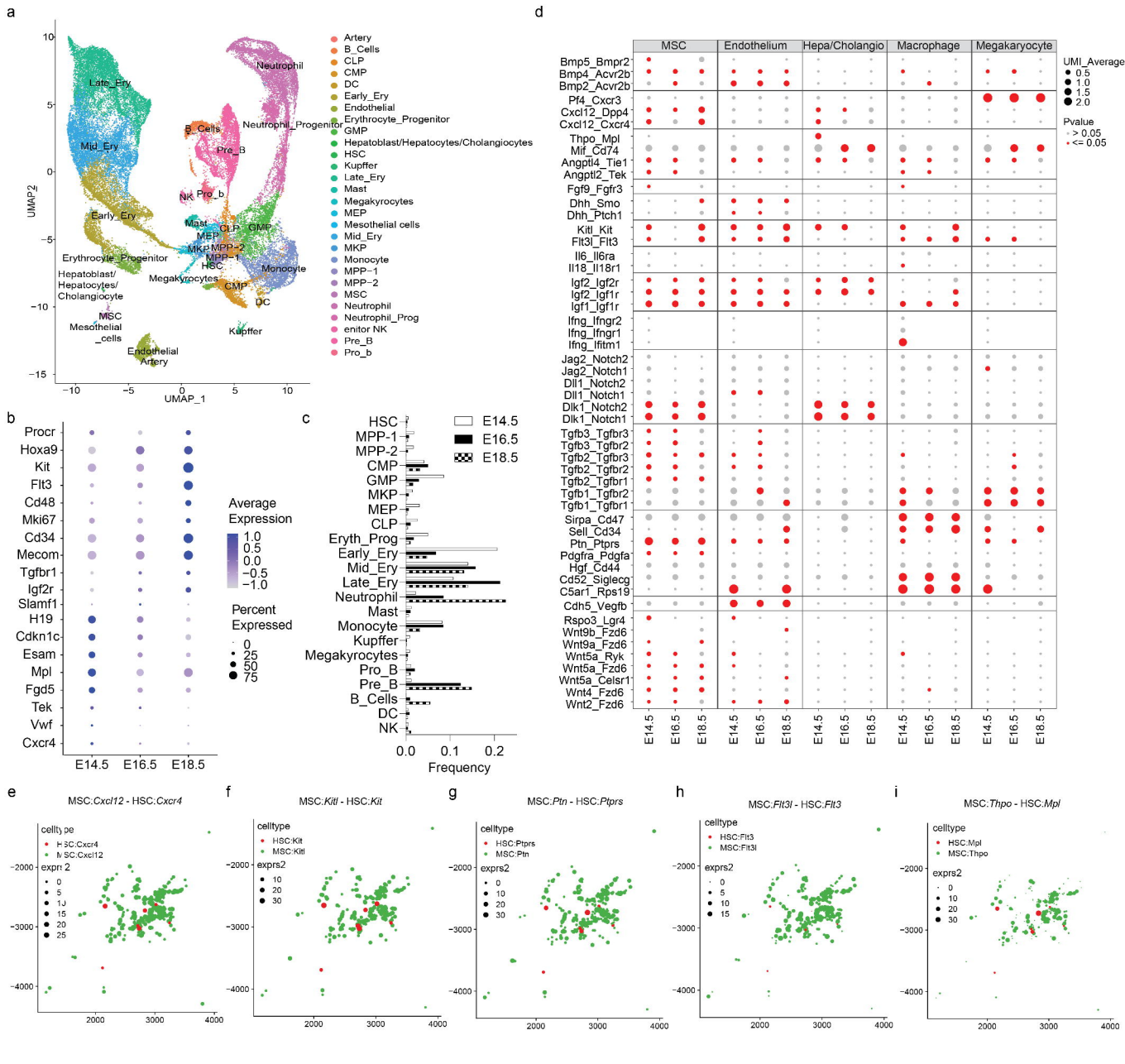
a
UMAP_1
UMAP2
Late_Ery
Mid_Ery
Early_Ery
Erythrocyte_Progenitor
Hepatoblast/
Hepatocytes/
Cholangiocyte
MSC
Mesothelial
_cells
Endothelial
Artery
Megakyrocytes
Mast
MEP
CLP
GMP
MKP
MPP-2
MPP-1
HSC
Monocyte
CMP
DC
Kupffer
Nk Pro_b
B_Cells
Pre_B
Neutrophil
Neutrophil_Progenitor
Artery
B_Cells
CLP
CMP
DC
Early_Ery
Endothelial
Erythrocyte_Progenitor
GMP
Hepatoblast/Hepatocytes/Cholangiocytes
HSC
Kupffer
Late_Ery
Mast
Megakyrocytes
MEP
Mesothelial cells
Mid_Ery
MKP
Monocyte
MPP-1
MPP-2
MSC
Neutrophil
Neutrophil_Prog
enitor NK
Pre_B
Pro_b
b
Procr
Hoxa9
Kit
Flt3
Cd48
Mki67
Cd34
Mecom
Tgfbr1
Igf2r
Slamf1
H19
Cdkn1c
Esam
Mpl
Fgd5
Tek
Vwf
Cxcr4
E14.5
E16.5
E18.5
Average
Expression
1.0
0.5
0.0
−0.5
−1.0
Percent
Expressed
0
25
50
75
c
HSC
MPP-1
MPP-2
CMP
GMP
MKP
MEP
CLP
Eryth_Prog
Early_Ery
Mid_Ery
Late_Ery
Neutrophil
Mast
Monocyte
Kupffer
Megakyrocytes
Pro_B
Pre_B
B_Cells
DC
NK
E14.5
E16.5
E18.5
Frequency
d
MSC
Endothelium
Hepa/Cholangio
Macrophage
Megakaryocyte
Bmp5_Bmpr2
Bmp4_Acvr2b
Bmp2_Acvr2b
Pf4_Cxcr3
Cxcl12_Dpp4
Cxcl12_Cxcr4
Thpo_Mpl
Mif_Cd74
Angptl4_Tie1
Angptl2_Tek
Fgf9_Fgfr3
Dhh_Smo
Dhh_Ptch1
Kitl_Kit
Flt3l_Flt3
Il6_Il6ra
Il18_Il18r1
Igf2_Igf2r
Igf2_Igf1r
Igf1_Igf1r
Ifng_Ifngr2
Ifng_Ifngr1
Ifng_Ifitm1
Jag2_Notch2
Jag2_Notch1
Dll1_Notch2
Dll1_Notch1
Dlk1_Notch2
Dlk1_Notch1
Tgfb3_Tgfbr3
Tgfb3_Tgfbr2
Tgfb2_Tgfbr3
Tgfb2_Tgfbr2
Tgfb2_Tgfbr1
Tgfb1_Tgfbr2
Tgfb1_Tgfbr1
Sirpa_Cd47
Sell_Cd34
Ptn_Ptprs
Pdgfra_Pdgfa
Hgf_Cd44
Cd52_Siglecg
C5ar1_Rps19
Cdh5_Vegfb
Rspo3_Lgr4
Wnt9b_Fzd6
Wnt9a_Fzd6
Wnt5a_Ryk
Wnt5a_Fzd6
Wnt5a_Celsr1
Wnt4_Fzd6
Wnt2_Fzd6
E14.5
E16.5
E18.5
UMI_Average
0.5
1.0
1.5
2.0
Pvalue
> 0.05
<= 0.05
e
MSC:Cxcl12 - HSC:Cxcr4
celltype
HSC:Cxcr4
MSC:Cxcl12
exprs2
f
MSC:Kitl - HSC:Kit
celltype
HSC:Kit
MSC:Kitl
exprs2
g
MSC:Ptn - HSC:Ptprs
celltype
HSC:Ptprs
MSC:Ptn
exprs2
h
MSC:Flt3l - HSC:Flt3
celltype
HSC:Flt3
MSC:Flt3l
exprs2
i
MSC:Thpo - HSC:Mpl
celltype
HSC:Mpl
MSC:Thpo
exprs2

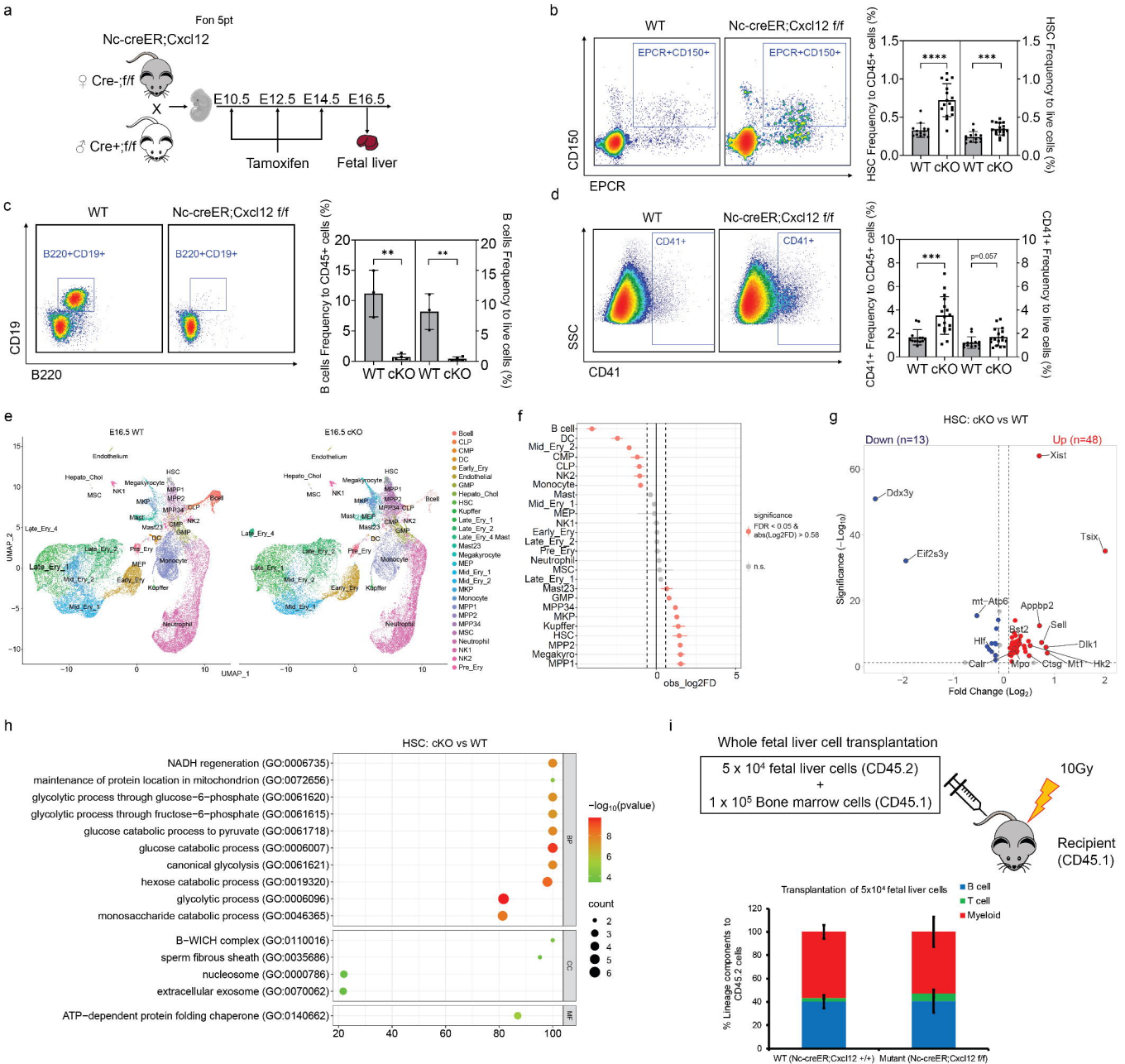
a
Fon 5pt
Nc-creER;Cxcl12
♀ Cre-;f/f
X
♂ Cre+;f/f
E10.5 E12.5 E14.5 E16.5
Tamoxifen
Fetal liver
b
WT
Nc-creER;Cxcl12 f/f
EPCR+CD150+
CD150
EPCR
HSC Frequency to CD45+ cells (%)
HSC Frequency to live cells (%)
****
***
WT cKO WT cKO
c
WT
Nc-creER;Cxcl12 f/f
B220+CD19+
CD19
B220
B cells Frequency to CD45+ cells (%)
B cells Frequency to live cells (%)
**
**
WT cKO WT cKO
d
WT
Nc-creER;Cxcl12 f/f
CD41+
SSC
CD41
CD41+ Frequency to CD45+ cells (%)
CD41+ Frequency to live cells (%)
***
p=0.057
WT cKO WT cKO
e
E16.5 WT
E16.5 cKO
UMAP_1
UMAP_2
Endothelium
Hepato_Chol
MSC
NK1
Megakyrocyte
HSC
MPP1
MPP2
MPP34
MKP
CLP
Bcell
Mast
Mast23
NK2
CMP
GMP
DC
Late_Ery_4
Late_Ery_2
Pre_Ery
Late_Ery_1
Mid_Ery_2
MEP
Early_Ery
Kupffer
Monocyte
Mid_Ery_1
Neutrophil
Bcell
CLP
CMP
DC
Early_Ery
Endothelial
GMP
Hepato_Chol
HSC
Kupffer
Late_Ery_1
Late_Ery_2
Late_Ery_4 Mast
Mast23
Megakyrocyte
MEP
Mid_Ery_1
Mid_Ery_2
MKP
Monocyte
MPP1
MPP2
MPP34
MSC
Neutrophil
NK1
NK2
Pre_Ery
f
B cell
DC
Mid_Ery_2
CMP
CLP
NK2
Monocyte
Mast
Mid_Ery_1
MEP
NK1
Early_Ery
Late_Ery_2
Pre_Ery
Neutrophil
MSC
Late_Ery_1
Mast23
GMP
MPP34
MKP
Kupffer
HSC
MPP2
Megakyro
MPP1
significance
FDR < 0.05 &
abs(Log2FD) > 0.58
n.s.
obs_log2FD
g
HSC: cKO vs WT
Down (n=13)
Up (n=48)
Xist
Ddx3y
Tsix
Eif2s3y
mt-Atp6
Apbbp2
Sell
Bst2
Hif
Dlk1
Calr
Mpo
Ctsg
Mt1
Hk2
Significance (−Log10)
Fold Change (Log2)
h
HSC: cKO vs WT
NADH regeneration (GO:0006735)
maintenance of protein location in mitochondrion (GO:0072656)
glycolytic process through glucose−6−phosphate (GO:0061620)
glycolytic process through fructose−6−phosphate (GO:0061615)
glucose catabolic process to pyruvate (GO:0061718)
glucose catabolic process (GO:0006007)
canonical glycolysis (GO:0061621)
hexose catabolic process (GO:0019320)
glycolytic process (GO:0006096)
monosaccharide catabolic process (GO:0046365)
B−WICH complex (GO:0110016)
sperm fibrous sheath (GO:0035686)
nucleosome (GO:0000786)
extracellular exosome (GO:0070062)
ATP−dependent protein folding chaperone (GO:0140662)
BP
CC
MF
−log10(pvalue)
count
i
Whole fetal liver cell transplantation
5 x 10⁴ fetal liver cells (CD45.2)
+
1 x 10⁵ Bone marrow cells (CD45.1)
10Gy
Recipient
(CD45.1)
Transplantation of 5x10⁴ fetal liver cells
B cell
T cell
Myeloid
% Lineage components to CD45.2 cells
WT (Nc-creER;Cxcl12 +/+)
Mutant (Nc-creER;Cxcl12 f/f)

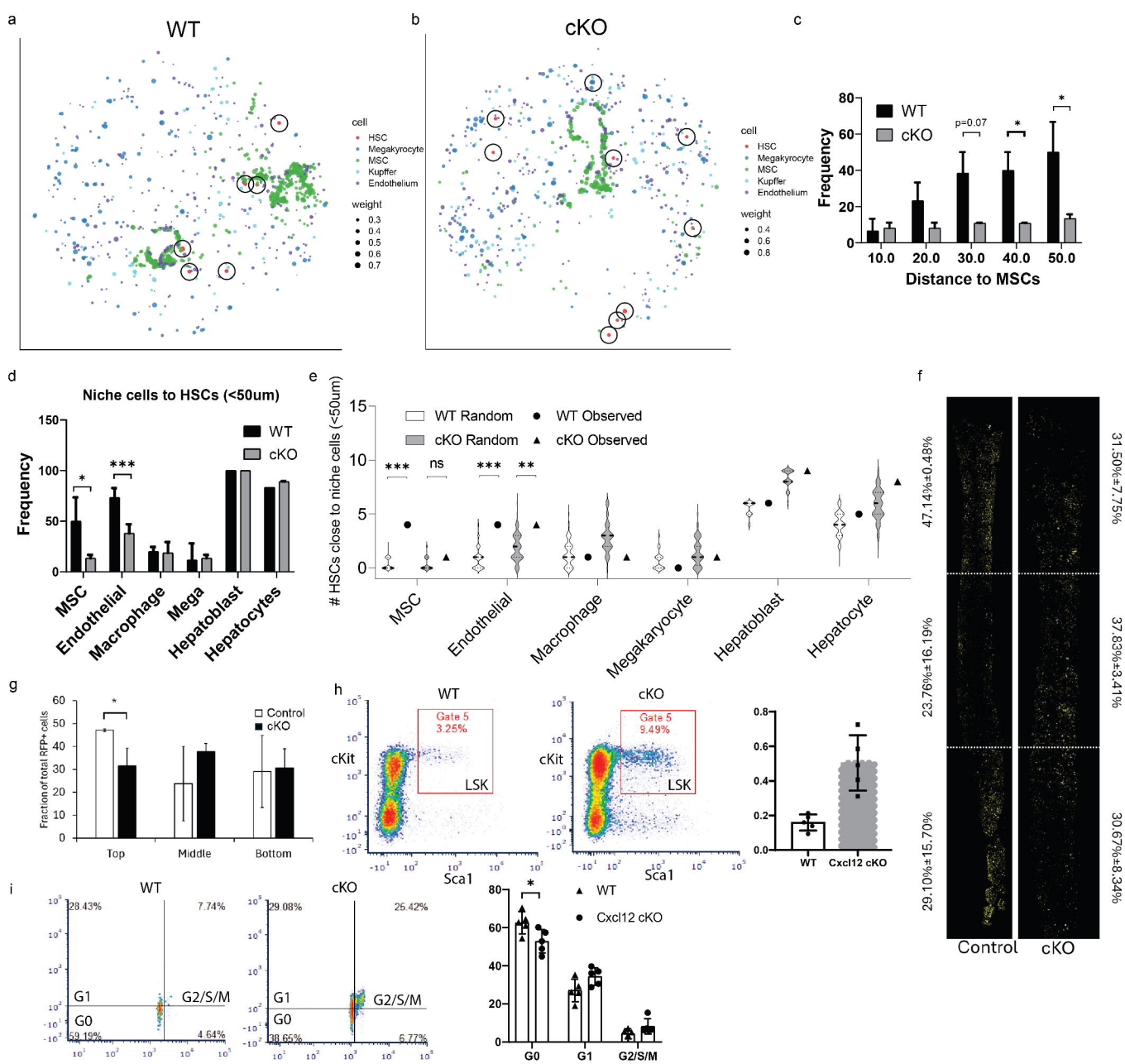
a
WT
cell
HSC
Megakyrocyte
MSC
Kupffer
Endothelium
weight
0.3
0.4
0.5
0.6
0.7
b
cKO
cell
HSC
Megakyrocyte
MSC
Kupffer
Endothelium
weight
0.4
0.6
0.8
c
WT
cKO
p=0.07
*
*
Frequency
Distance to MSCs
10.0
20.0
30.0
40.0
50.0
d
Niche cells to HSCs (<50um)
WT
cKO
Frequency
MSC
Endothelial
Macrophage
Mega
Hepatoblast
Hepatocytes
e
WT Random
cKO Random
WT Observed
cKO Observed
HSCs close to niche cells (<50um)
ns
MSC
Endothelial
Macrophage
Megakaryocyte
Hepatoblast
Hepatocyte
f
47.14%±0.48%
23.76%±16.19%
29.10%±15.70%
31.50%±7.75%
37.83%±3.41%
30.67%±8.34%
Control
cKO
g
Control
cKO
Fraction of total RFP+ cells
Top
Middle
Bottom
h
WT
cKO
Gate 5
3.25%
Gate 5
9.49%
cKit
LSK
Sca1
WT
Cxcl12 cKO
i
WT
cKO
28.43%
7.74%
G1
G2/S/M
G0
59.19%
4.64%
29.08%
25.42%
38.65%
6.77%
WT
Cxcl12 cKO
G0
G1
G2/S/M